SIAM J. IMAGING SCIENCES
Vol. 12, No. 3, pp. 1275–1295

A Learning-Based Method for Solving Ill-Posed Nonlinear Inverse Problems: A Simulation Study of Lung EIT*

Jin Keun Seo†, Kang Cheol Kim†, Ariungerel Jargal†, Kyounghun Lee†, and Bastian Harrach‡

Abstract. This paper proposes a new approach for solving ill-posed nonlinear inverse problems. For ease of explanation of the proposed approach, we use the example of lung electrical impedance tomography (EIT), which is known to be a nonlinear and ill-posed inverse problem. Conventionally, penalty-based regularization methods have been used to deal with the ill-posed problem. However, experiences over the last three decades have shown methodological limitations in utilizing prior knowledge about tracking expected imaging features for medical diagnosis. The proposed method's paradigm is completely different from conventional approaches; the proposed reconstruction uses a variety of training data sets to generate a low dimensional manifold of approximate solutions, which allows conversion of the ill-posed problem to a well-posed one. Variational autoencoder was used to produce a compact and dense representation for lung EIT images with a low dimensional latent space. Then, we learn a robust connection between the EIT data and the low dimensional latent data. Numerical simulations validate the effectiveness and feasibility of the proposed approach.

Key words. electrical impedance tomography, deep learning, variational autoencoder, inverse problems

AMS subject classification. 35R30

DOI. 10.1137/18M1222600

1. Introduction.

Electrical impedance tomography (EIT) aims to provide tomographic images of an electrical conductivity distribution inside an electrically conducting object such as the human body [6, 9, 5, 25, 26, 52]. In EIT, we attach an array of surface electrodes around a chosen imaging slice of the object to inject currents and measure the induced voltages. Noting that current-voltage relation reflects the conductivity distribution according to Ohm's law, an accurate conductivity reconstruction by EIT is theoretically possible [4, 10, 30, 34, 46, 47, 55].

However, EIT in a clinical setting has suffered from the fundamental limitations that current-voltage data is very sensitive to the forward modeling errors involving the boundary geometry and the electrode configuration, whereas it is insensitive to local perturbation of the conductivity. Since the inverse problem of EIT is highly ill-posed, the most common techniques are regularized model-fitting approaches (e.g., least square minimization combined with

---

*Received by the editors October 24, 2018; accepted for publication (in revised form) April 23, 2019; published electronically July 2, 2019.

https://doi.org/10.1137/18M1222600

Funding: The work of the first and second authors was supported by the National Research Foundation of Korea (NRF) grants 2015R1A5A1009350 and 2017R1A2B20005661. The work of the third and fourth authors was supported by the National Research Foundation of Korea (NRF) grant 2017R1E1A1A03070653.

†Department of Computational Science and Engineering, Yonsei University, Seoul, 120-749, Korea (seoj@yonsei.ac.kr, kangcheol@yonsei.ac.kr, j.ariungerel@gmail.com, imlkh84@gmail.com).

‡Department of Mathematics, Goethe University Frankfurt, 60325 Frankfurt am Main, Germany (harrach@math.uni-frankfurt.de).

regularization) [13, 40]. Unfortunately, in a clinical environment, these techniques have not provided satisfactory results in terms of accuracy and resolution despite numerous endeavors in the last four decades. Within conventional regularization frameworks, including Tikhonov [56] and total variation regularization, it seems to be very difficult to enforce prior knowledge of possible solutions effectively.

This paper suggests a new paradigm of EIT reconstruction using a specially designed deep learning framework to leverage prior knowledge of solutions. For ease of explanation, this paper focuses on the mathematical model of the time-difference EIT imaging of air ventilation in the lungs. We denote by $\gamma_t(\mathbf{r})$ the conductivity at time t and position $\mathbf{r}$. The input data for the deep learning is the time-difference of the current-voltage data $\dot{\mathbf{V}}_t := \mathbf{V}_t - \mathbf{V}_{t_0}$ in EIT (see section 2 for $\dot{\mathbf{V}}$), and the output is the difference conductivity image $\dot{\gamma}_t := \gamma_t - \gamma_{t_0}$, where t_0 denotes a reference time. With fixing time t, we will use the shorter notations $\dot{\gamma}$ and $\dot{\mathbf{V}}$ instead of $\dot{\gamma}_t$ and $\dot{\mathbf{V}}_t$, respectively. The goal is to learn an EIT reconstruction map f_{EIT} from training data set $\{(\dot{\mathbf{V}}^n, \dot{\gamma}^n) : n = 1, \ldots, N\}$ such that $f_{\text{EIT}}(\dot{\mathbf{V}})$ produces a useful reconstruction for $\dot{\gamma}$.

The standard deep learning paradigm is to learn a reconstruction function $f_{\text{EIT}} : \dot{\mathbf{V}} \mapsto \dot{\gamma}$ using many training data $\{(\dot{\mathbf{V}}^n, \dot{\gamma}^n) : n = 1, \ldots, N\}$. The main issue is to find a suitable deep learning network ($\mathbb{DL}$) which allows learning of a useful reconstruction map f_{EIT} from

$$f_{\text{EIT}} = \underset{f \in \mathbb{DL}}{\operatorname{argmin}} \frac{1}{N} \sum_{n=1}^{N} \| f(\dot{\mathbf{V}}^n) - \dot{\gamma}^n \|^2. \tag{1}$$

The deep learning-based reconstruction method exploits an integrated knowledge synthesis from the training data in order to get a direct reconstruction $\dot{\gamma} = f_{\text{EIT}}(\dot{\mathbf{V}})$ from a new measurement $\mathbf{V}$.

The deep learning method is very different from the conventional regularized model-fitting method, which can be expressed as

$$\dot{\gamma} = \underset{\dot{\gamma} \in \mathcal{H}}{\operatorname{argmin}} \| \dot{\mathbf{V}} - \mathbb{S}\dot{\gamma} \|^2 + \lambda \mathit{Reg}(\dot{\gamma}), \tag{2}$$

where $\mathbb{S} \approx \frac{\partial \dot{\mathbf{V}}}{\partial \dot{\gamma}}$ is the Jacobian matrix or sensitivity matrix (see section 2.1 for details), $\mathit{Reg}(\dot{\gamma})$ is the regularization term enforcing the regularity of $\dot{\gamma}$, and λ is the regularization parameter controlling the trade-off between the residual norm and regularity. Here, $\mathcal{H}$ is a space for representing images. In the case when the total number of pixels in the image is d, $\mathcal{H} = \mathbb{R}^d$. Since the dimension of $\mathcal{H}$ mostly is much bigger than the number of independent components in the measurement data $\dot{\mathbf{V}}$, a large number of possible images are consistent with the measurements up to the model and measurement error. Regularization is used to incorporate a priori information in order to choose the image for which the regularization functional is smallest. The success of this approach depends on whether the regularization term is indeed a good indicator for realistic lung images. In order to improve image quality, it seems desirable to go beyond standard regularization frameworks and add more specific a priori information.

In this work, we propose to use a deep learning method to find a useful constraint on EIT solutions for the lung ventilation model. We use a variational autoencoder learning technique (or manifold learning approach) to get a nonlinear expression of practically meaningful solutions $\dot{\gamma}$ by variables $\mathbf{h}$ in a low dimensional latent space; i.e., a decoder Ψ is learned from training data to get the nonlinear representation $\dot{\gamma} = \Psi(\mathbf{h})$. This generates the tripled training data $\{(\dot{\mathbf{V}}^n, \dot{\gamma}^n, \mathbf{h}^n) : n = 1, \dots, N\}$. Next, we use the training data to learn a nonlinear regression map $f_{\mathrm{Vh}} : \dot{\mathbf{V}} \to \mathbf{h}$, which makes a connection between the latent variables $\mathbf{h}$ and the data $\dot{\mathbf{V}}$. The nonlinear regression map f_{Vh} is obtained by

$$f_{\mathrm{Vh}} = \operatorname*{argmin}_{f_{\mathrm{Vh}} \in \mathbb{DL}_h} \frac{1}{N} \sum_{n=1}^{N} \| f_{\mathrm{Vh}}(\dot{\mathbf{V}}^n) - \mathbf{h}^n \|^2, \tag{3}$$

where $\mathbb{DL}_h$ is a deep learning network described in section 2.3. Then, the reconstruction map f_{EIT} is expressed as $f_{\mathrm{EIT}} = \Psi \circ f_{\mathrm{Vh}}$. The feasibility of the proposed method is demonstrated by using numerical simulations. The performance can be enhanced by accumulating high quality training data (clinically useful EIT images).

Before closing this introduction, we should mention that our method does not use *ground-truth* labeled data for training because lung EIT lacks a known ground truth at present. Although we have collected many human experiment data using a 16-channel EIT system [39], its ground truthiness is not clear from a clinical point of view. Phantom experimental results cannot be used for ground-truth data, which are far from realistic. The collection of ground-truth training data may require a tough and complex process involving expensive clinical trials. The issue of collecting training data is beyond the scope of this paper.

2. Time-difference EIT and conventional reconstruction methods.

2.1. Time-difference EIT. We briefly explain the mathematical model of an E-channel time-difference EIT system in which $E \in \mathbb{N}$ electrodes are placed around the human thorax. See Figure 1 for a sketch of a 16-channel EIT system. We assume that measurements are taken in the following adjacent-adjacent pattern. A current of strength I is driven through the jth pair of adjacent electrodes $(\mathcal{E}^j, \mathcal{E}^{j+1})$, keeping all other electrodes insulated, where we use the convention that $\mathcal{E}^{E+1} = \mathcal{E}^1$. Then the resulting electric potential u_t^j satisfies approximately the shunt model equations (ignoring the contact impedances underneath the electrodes):

$$\begin{cases} \nabla \cdot (\gamma_t \nabla u_t^j) = 0 & \text{in } \Omega, \\ \int_{\mathcal{E}^j} \gamma \nabla u_t^j \cdot \mathbf{n}\, ds = I = -\int_{\mathcal{E}^{j+1}} \gamma \nabla u_t^j \cdot \mathbf{n}\, ds, & \\ (\gamma_t \nabla u_t^j) \cdot \mathbf{n} = 0 & \text{on } \partial\Omega \setminus \cup_i^E \mathcal{E}^i, \\ \int_{\mathcal{E}^i} \gamma_t \nabla u_t^j \cdot \mathbf{n} = 0 & \text{for } i \in \{1, \dots, E\} \setminus \{j, j+1\}, \\ u_t^j|_{\mathcal{E}^i} = \text{const.} & \text{for } i = 1, \dots, E, \\ \sum_{i=1}^{E} u_t^j|_{\mathcal{E}^i} = 0, & \end{cases} \tag{4}$$

where γ_t is the conductivity distribution inside the imaging domain Ω at time t, $\mathbf{n}$ is the outward unit normal vector to $\partial\Omega$, and ds is the surface element.

Driving the current through the jth pair of adjacent electrodes, we measure the voltage difference between the kth pair of adjacent electrodes

$$V_t^{jk} = u_t^j|_{\mathcal{E}^k} - u_t^j|_{\mathcal{E}^{k+1}}.$$

We measure V_t^{jk} for all combinations of $j, k \in \{1, \dots, E\}$ excluding voltage measurements on current-driven electrodes since they are known to be highly affected by skin-electrode contact impedance, which is ignored in the shunt model [21] for a possible remedy. Thus the EIT measurements at time t are given by the $E(E-3)$-dimensional vector

$$\mathbf{V}_t = (V_t^{1,3}, \ldots, V_t^{1,E-1}, V_t^{2,4}, \ldots, V_t^{2,E}, \ldots, V_t^{E,2}, \ldots, V_t^{E,E-2})^T \in \mathbb{R}^{E(E-3)},$$

where the superscript T stands for the transpose of the vector.

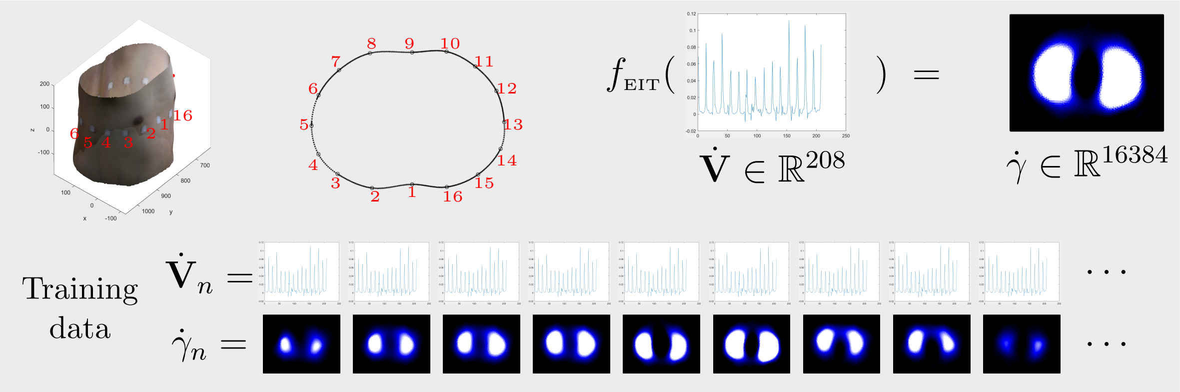

Figure 1. *16-channel EIT system for monitoring regional lung ventilation. 16 electrodes are attached around the thorax to inject currents and measure boundary voltages. The set of current-voltage data (i.e., a discrete version of Neumann-to-Dirichlet data) is used to reconstruct time-difference conductivity images.*

In time-difference EIT, we use the difference of two measurements

$$\dot{\mathbf{V}} := \mathbf{V}_t - \mathbf{V}_{t_0} \in \mathbb{R}^{E(E-3)} \tag{5}$$

between sampling time t and reference time t_0 in order to provide an image of the conductivity difference

$$\dot{\gamma} := \gamma_t - \gamma_{t_0}.$$

From the variational formulation of (4), one obtains the following linear approximation:

$$\begin{aligned} \dot{V}^{jk} &:= V_t^{jk} - V_{t_0}^{jk} = \tfrac{1}{I}\int_\Omega \left[\gamma_t \nabla u_t^j \cdot \nabla u_t^k - \gamma_{t_0} \nabla u_{t_0}^j \cdot \nabla u_{t_0}^k\right] d\mathbf{r} \\ &\approx \tfrac{1}{I}\int_\Omega \dot{\gamma} \nabla u_{t_0}^j \cdot \nabla u_{t_0}^k \, d\mathbf{r}. \end{aligned} \tag{6}$$

For a computerized image reconstruction, we discretize Ω into finite elements Δ_m, $m = 1, 2, \ldots, d$, as $\Omega \approx \cup_{m=1}^d \Delta_m$, and assume that $\dot{\gamma}$ is approximately constant on each element Δ_m. Let $\dot{\gamma}_m \in \mathbb{R}$ denote the value of $\dot{\gamma}$ on Δ_m and identify $\dot{\gamma}$ with the column vector

$$\dot{\gamma} = (\dot{\gamma}_1, \ldots, \dot{\gamma}_d)^T \in \mathbb{R}^d.$$

Then (6) can be written as

$$\dot{V}^{jk} \approx \sum_{m=1}^{d} s_{jk}^m \dot{\gamma}_m \quad \text{with } s_{jk}^m := \frac{1}{I}\int_{\Delta_m} \nabla u_{t_0}^j \cdot \nabla u_{t_0}^k \, d\mathbf{r}.$$

To write this in matrix-vector form, we fix $m = 1, \dots, d$ and write the elements of s^m_{jk} as a $E(E-3)$-dimensional vector

$$\mathbf{S}^m = \left(s^m_{1,3}, \dots, s^m_{1,E-1}, s^m_{2,4}, \dots, s^m_{2,E}, \dots, s^m_{E,2}, \dots, s^m_{E,E-2}\right)^T \in \mathbb{R}^{E(E-3)}. \tag{7}$$

Using these vectors as columns, we define the sensitivity matrix $\mathbb{S} \in \mathbb{R}^{E(E-3)\times d}$ and can thus write (6) as

$$\dot{\mathbf{V}} \approx \sum_{m=1}^{d} \dot{\gamma}_m \mathbf{S}^m = \begin{pmatrix} | & & | \\ \mathbf{S}^1 & \cdots & \mathbf{S}^d \\ | & & | \end{pmatrix} \begin{pmatrix} \dot{\gamma}_1 \\ \vdots \\ \dot{\gamma}_d \end{pmatrix} = \mathbb{S}\,\dot{\gamma}. \tag{8}$$

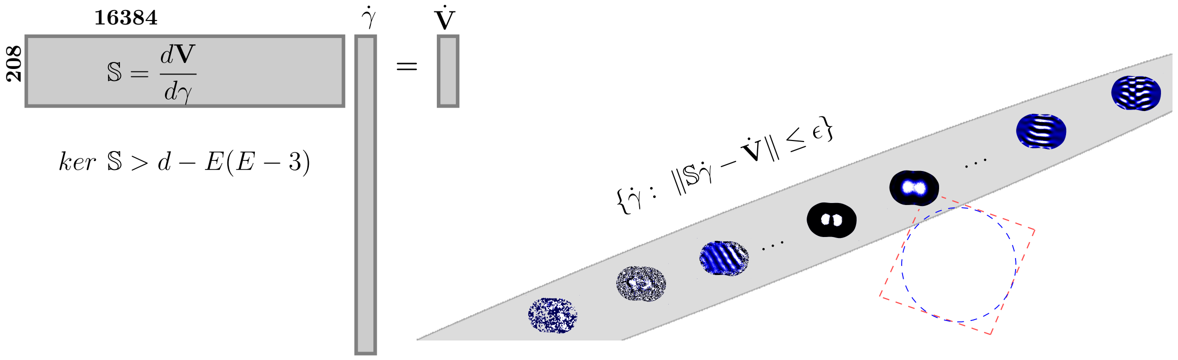

Figure 2. *The system $\mathbb{S}\dot{\gamma} = \dot{\mathbf{V}}$ on the left figure is a highly underdetermined problem. The set $Sol_\epsilon(\dot{\mathbf{V}})$ in (9) can be viewed as an ϵ-neighborhood of a space with dimension more than 16000. The image on the right describes conventional penalty-based regularization methods that select an image from the set $Sol_\epsilon(\dot{\mathbf{V}})$.*

2.2. Conventional penalty-based regularization methods. In most practical applications, d (the total number of pixels for $\dot{\gamma}$) is much bigger than $E(E-3)$ (the number of measurements), so that the linearized problem $\mathbb{S}\dot{\gamma} = \dot{\mathbf{V}}$ is a highly underdetermined system. When a 16-channel EIT system is used to produce images with 128 × 128 pixels, then the kernel dimension of $\mathbb{S}$ is at least $128^2 - 16 * 13$, so that a solution of $\mathbb{S}\dot{\gamma} = \dot{\mathbf{V}}$ is only unique up to addition of an image coming from a more than 16000-dimensional vector space.

Moreover, the linearized problem is only a rough approximation of the real situation, and the measurements contain unavoidable noises. Hence, all conductivity distributions $\dot{\gamma}$ in the wide region

$$Sol_\epsilon(\dot{\mathbf{V}}) := \{\dot{\gamma} \in \mathbb{R}^d \ : \ \|\mathbb{S}\dot{\gamma} - \dot{\mathbf{V}}\|_{\text{fid}} \leq \epsilon\} \tag{9}$$

have to be regarded as consistent with the measurements, where ϵ is a tolerance reflecting modeling and measurement errors, and $\|\cdot\|_{\text{fid}}$ is a norm measuring the data fidelity. In the following we simply use $\|\cdot\|_2$ as the fidelity norm.

Conventional penalty-based regularization methods reconstruct the conductivity image by choosing $\dot{\gamma}$ from all consistent candidates in $Sol_\epsilon(\dot{\mathbf{V}})$, so that it is smallest in some norm that penalizes unrealistic results; cf. Figure 2. Popular approaches include the simple Euclidean norm and the total variation norm, which lead to the minimization problems

$$\dot{\gamma} = \underset{\dot{\gamma}}{\operatorname{argmin}} \|\dot{\mathbf{V}} - \mathbb{S}\dot{\gamma}\|_2^2 + \lambda \|\dot{\gamma}\|_2^2 \tag{10}$$

and

$$\dot{\gamma} = \underset{\dot{\gamma}}{\operatorname{argmin}} \|\dot{\mathbf{V}} - \mathbb{S}\dot{\gamma}\|^2 + \lambda \|D\dot{\gamma}\|_1, \tag{11}$$

where $\lambda > 0$ is a regularization parameter and $D\dot{\gamma}$ is the discretized gradient of $\dot{\gamma}$.

The performance of these approaches depends on whether the norm in the penalization term is indeed a good indicator for realistic images. In order to improve image quality, it seems desirable to add more specific a priori information.

2.3. Generic deep learning-based method.

Generic deep learning methods or lung monitoring in an E-channel EIT system rely on a training data set of conductivity images and voltage measurements

$$\{(\dot{\gamma}_n, \dot{\mathbf{V}}_n) \in \mathbb{R}^d \times \mathbb{R}^{E(E-3)} : \ n = 1, \dots, N\}$$

and aim to learn a useful reconstruction map f_{EIT} from a suitable class of functions described by a deep learning network $\mathbb{DL}$ through the minimization problem

$$f_{\text{EIT}} = \underset{f \in \mathbb{DL}}{\operatorname{argmin}} \frac{1}{N} \sum_{n=1}^{N} \|f(\dot{\mathbf{V}}_n) - \dot{\gamma}_n\|^2. \tag{12}$$

By using a training set, these methods incorporate very problem-specific a priori information. But they do not explicitly take into account that the EIT reconstruction problem is highly underdetermined and ill-posed.

3. A manifold learning-based image reconstruction method.

3.1. Motivation: Adding a manifold constraint.

To solve the highly underdetermined system $\mathbb{S}\dot{\gamma} = \dot{\mathbf{V}}$, we follow the new paradigm that realistic lung images lie on a nonlinear manifold that is much lower dimensional than the space of all possible images. If we can identify a suitable set $\mathcal{M}$ including images representing lung ventilation, then we can solve the constrained problem

$$\left\| \begin{array}{l} \text{Solve } \ \mathbb{S}\dot{\gamma} \ \approx \ \dot{\mathbf{V}} \\ \text{subject to the constraint } \dot{\gamma} \in \mathcal{M}. \end{array} \right. \tag{13}$$

The unknown constraint $\mathcal{M}$ is hoped to be a low dimensional manifold of images displaying lung ventilation such that the intersection $\mathcal{M} \cap Sol_\epsilon(\dot{\mathbf{V}})$ is nonempty and of small diameter. With this $\mathcal{M}$, it is hoped that the constraint problem is "approximately well-posed" in the following approximate version of the Hadamard well-posedness [19]:

(a) *Approximate uniqueness and stability.* If two images $\dot{\gamma}, \dot{\gamma}' \in \mathcal{M}$ satisfy $\mathbb{S}\dot{\gamma} \approx \mathbb{S}\dot{\gamma}'$, then $\dot{\gamma} \approx \dot{\gamma}'$.

(b) *Approximate existence.* For any lung EIT data $\dot{\mathbf{V}}$, there exist $\dot{\gamma} \in \mathcal{M}$ such that $\mathbb{S}\dot{\gamma} \approx \dot{\mathbf{V}}$.

Many new theoretical and practical problems arise with this new paradigm. How to identify and describe manifolds displaying lung ventilation on which the constrained inverse problem (13) is robustly solvable is a highly challenging question. A recent step in this direction is the result in [22] which shows that the inverse problem of EIT with sufficiently many electrodes is uniquely solvable and Lipschitz stable on finite dimensional linear subsets of piecewise-analytic functions.

3.2. Well-posedness of the inverse conductivity problem on compact sets.

The average image $\frac{\dot{\gamma}^1+\dot{\gamma}^2}{2}$ of two different images $\dot{\gamma}^1$ and $\dot{\gamma}^2$ displaying lung ventilation may not be a useful representation of lung ventilation. Hence, it is desirable to work with low dimensional nonlinear manifolds for the conductivity image rather than with low dimensional vector spaces. As a first result to show that the inverse conductivity can be approximately well-posed under nonlinear constraints, we will now show that the inverse conductivity problem with continuous measurements (modeled by the Neumann–Dirichlet operator) uniformly continuously determines the conductivity in compact sets of piecewise-analytic functions. We expect that the result also holds for voltage measurements on a sufficiently high number of electrodes, though that would require results on the approximation of the Neumann–Dirichlet operator with the shunt electrode model that are outside the scope of this work.

For the following result let us also stress that the unique solvability of the inverse conductivity problem for piecewise-analytic conductivity functions and the continuum model is a classical result from Kohn and Vogelius [34, 35]. Without further restriction, the inverse conductivity problem is highly ill-posed, and due to the nonlinearity, stability is not a trivial consequence of restricting the conductivity to compact subsets. Alessandrini and Vessella [3] have proven Lipschitz stability for the continuum model when the conductivity belongs to an a priori known bounded subset of a finite dimensional linear subspace of C^2-functions, and [22] shows Lipschitz stability for bounded subsets of finite dimensional linear subspace of piecewise-analytic functions for the complete electrode model with sufficiently many electrodes. The following result follows the ideas from [24, 22] (see also [23]) to show that stability holds on any (possibly nonlinear) compact subset of piecewise-analytic functions. It indicates that our new approach of constructing a low dimensional nonlinear manifold of useful lung images may indeed convert the ill-posed problem into a well-posed one.

Theorem 1. *Let $C \subseteq L^\infty_+(\Omega)$ be a compact set of piecewise analytic functions (in the sense of [35]). For $\gamma \in C$ let $\Lambda(\gamma)$ denote the Neumann–Dirichlet operator, i.e.,*

$$\Lambda(\gamma): \ L^2_\diamond(\partial\Omega) \to L^2_\diamond(\partial\Omega), \quad g \mapsto u|_{\partial\Omega},$$

where $u \in H^1_\diamond(\Omega)$ solves $\nabla \cdot (\gamma \nabla u) = 0$ in Ω.

Then for all $\epsilon > 0$ there exists $\delta > 0$ so that for all $\gamma_1, \gamma_2 \in C$

$$\|\Lambda(\gamma_1) - \Lambda(\gamma_2)\| < \delta \quad \textit{implies} \quad \|\gamma_1 - \gamma_2\| < \epsilon.$$

Proof. Let $\epsilon > 0$. As in [22], we have that for all $\gamma_1, \gamma_2 \in C$ with $\|\gamma_1 - \gamma_2\| \geq \epsilon$

$$\begin{aligned}\|\Lambda(\gamma_1) - \Lambda(\gamma_2)\| &\geq \sup_{g \in L^2_\diamond(\partial\Omega),\ \|g\|=1} f(\gamma_1, \gamma_2, \gamma_2 - \gamma_1, g) \\ &\geq \inf_{\tau_1, \tau_2 \in C,\ \kappa \in K} \sup_{g \in L^2_\diamond(\partial\Omega),\ \|g\|=1} f(\tau_1, \tau_2, \kappa, g),\end{aligned}$$

where f is defined by taking the maximum of two values arising from monotonicity inequalities in [22],

$$\begin{aligned} f:\ L^\infty_+(\Omega) \times L^\infty_+(\Omega) \times L^\infty(\Omega) \times L^2_\diamond(\partial\Omega) \to \mathbb{R}, \\ f(\tau_1, \tau_2, \kappa, g) := \max\{\langle(\Lambda'(\tau_1)\kappa)g, g\rangle, -\langle(\Lambda'(\tau_2)\kappa)g, g\rangle\},\end{aligned}$$

and

$$K := \{\kappa = \tau_1 - \tau_2 :\ \tau_1, \tau_2 \in C,\ \|\tau_1 - \tau_2\| \geq \epsilon\}.$$

From the compactness of C, it easily follows that K is also compact. The function

$$(\tau_1, \tau_2, \kappa) \mapsto \sup_{g \in L^2_\diamond(\partial\Omega),\ \|g\|=1} f(\tau_1, \tau_2, \kappa, g)$$

is lower semicontinuous (see [22]) and thus attains its minimum over the compact set $C \times C \times K$. With the same arguments as in [22, Lemma 2.11] it follows that

$$\sup_{g \in L^2_\diamond(\partial\Omega),\ \|g\|=1} f(\tau_1, \tau_2, \kappa, g) > 0 \quad \text{for all } (\tau_1, \tau_2, \kappa) \in C \times C \times K,$$

so that we obtain

$$\delta := \inf_{\tau_1, \tau_2 \in C,\ \kappa \in K} \sup_{g \in L^2_\diamond(\partial\Omega),\ \|g\|=1} f(\tau_1, \tau_2, \kappa, g) > 0.$$

Hence,

$$\|\Lambda(\gamma_1) - \Lambda(\gamma_2)\| \geq \delta \quad \text{for all} \quad \gamma_1, \gamma_2 \in C \text{ with } \|\gamma_1 - \gamma_2\| \geq \epsilon,$$

so that the assertion follows by contraposition. ■

3.3. Filtered data. Before we aim to find a manifold representation of lung ventilation images, we preprocess the voltage measurements to remove geometry modeling errors. In practical lung EIT, it is cumbersome to take account of patient-to-patient variability in terms of the boundary geometry and electrode positions, and it requires considerable effort to accurately estimate geometry information. Moreover, the voltage measurements $\dot{\mathbf{V}}$ can be affected by respiratory motion artifacts. Hence, it is desirable to filter out these boundary uncertainties as much as possible to extract a ventilation-related signal, denoted by $\dot{\mathbf{V}}_{\text{lung}}$.

To this end, we preprocess the voltage measurements as in [39]. We extract the boundary error, denoted by $\dot{\mathbf{V}}_{\text{err}}$, by using the boundary sensitive Jacobian matrix $\mathbb{S}_{\text{bdry}}$:

$$\dot{\mathbf{V}}_{\text{err}} := \mathbb{S}_{\text{bdry}} \left(\mathbb{S}^T_{\text{bdry}} \mathbb{S}_{\text{bdry}} + \lambda \mathbb{I}\right)^{-1} \mathbb{S}^T_{\text{bdry}} \dot{\mathbf{V}},$$

where λ is a regularization parameter, $\mathbb{I}$ is the identity matrix, and $\mathbb{S}_{\rm bdry}$ is a submatrix of $\mathbb{S}$ consisting of all columns corresponding to the triangular elements located adjacent to the boundary. Then, the filtered data $\dot{\mathbf{V}}_{\rm lung} = \dot{\mathbf{V}} - \dot{\mathbf{V}}_{\rm err}$ is not so sensitive to the boundary $\partial\Omega$ and motion artifacts [39].

From now on, we use this filtered data $\dot{\mathbf{V}}_{\rm lung}$ for the reconstruction instead of $\dot{\mathbf{V}}$ in order to alleviate the boundary error and motion artifacts. For notational simplicity, we use the same notation $\dot{\mathbf{V}}$ for the filtered data $\dot{\mathbf{V}}_{\rm lung}$.

3.4. Low dimensional manifold representation. Assume that we are given a training data set of conductivity images and voltage measurements from an E-channel EIT system

$$\{(\dot{\gamma}_n, \dot{\mathbf{V}}_n) \in \mathbb{R}^d \times \mathbb{R}^{E(E-3)} : \ n = 1, \dots, N\}.$$

Instead of directly applying a generic deep learning approach as described in subsection 2.3, we follow the new paradigm described in subsection 3.1 that images of lung ventilation lie on a low dimensional manifold $\mathcal{M}$ on which the inverse problem is approximately well-posed.

We therefore first use the conductivity images in the training data set

$$\{\dot{\gamma}_n \in \mathbb{R}^d : \ n = 1, \dots, N\}$$

to generate the low dimensional manifold $\mathcal{M}$. In an E-channel EIT system, the number of independent information in the measured current-voltage data is at most $E(E-3)/2$ due to the reciprocity $\dot{V}^{ji} = \dot{V}^{ij}$. Hence, in order to make the inverse problem approximately well-posed, we aim to generate $\mathcal{M}$ with dimension less than $E(E-3)/2$.

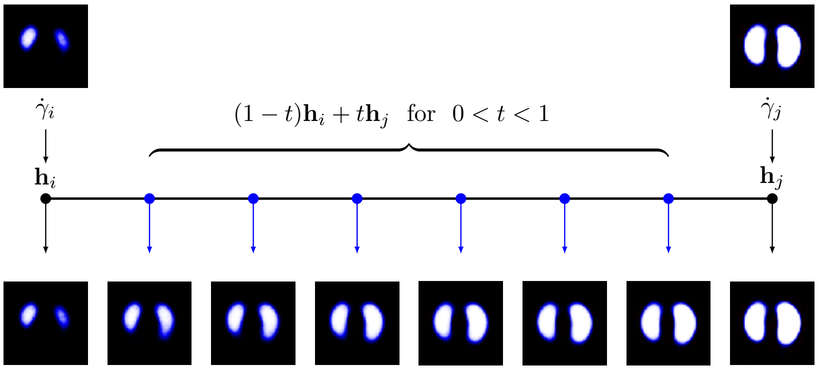

Figure 3. *Interpolation between two points* $\mathbf{h}_i$ *and* $\mathbf{h}_j$ *in the latent space. Given two images* $\dot{\gamma}_i = \Psi(\mathbf{h}_i)$ *and* $\dot{\gamma}_j = \Psi(\mathbf{h}_j)$*, VAE allows one to generate the interpolated image* $\Psi((1-t)\mathbf{h}_i + t\mathbf{h}_j)$ *for* $0 < t < 1$.

3.4.1. Autoencoder. Given a data set of lung EIT images, a variational autoencoder (VAE) [32] technique is used to learn the distribution of lung EIT images with the assumption that lung EIT image data (high dimensional) actually lies on a low dimensional manifold $\mathcal{M}$. For ease of explanation of our idea, we start by first explaining the proposed method with the well-known standard autoencoder instead of VAE. Autoencoder uses the training data set $\{\dot{\gamma}_n \in \mathbb{R}^d : \ n = 1, \dots, N\}$ to learn two functions (called encoder and decoder)

$$\Phi : \ \mathbb{R}^d \to \mathbb{R}^k \quad \text{and} \quad \Psi : \ \mathbb{R}^k \to \mathbb{R}^d$$

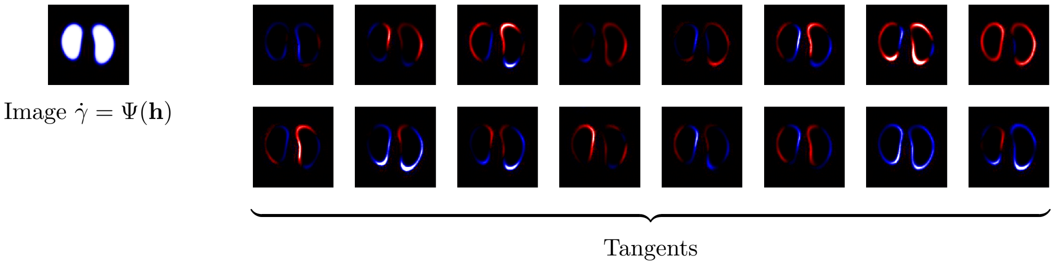

Figure 4. *Tangent vector of $\mathcal{M}$. Assuming that $\dot\gamma = \Psi(\mathbf{h})$ is the image on the top left, its gradient $\nabla\Psi(\mathbf{h})$ can be expressed as the images on the right side.*

from a class of functions $\mathbb{AE}$ described by a deep learning network by minimizing

$$(\Psi, \Phi) = \underset{(\Psi,\Phi)\in\mathbb{AE}}{\operatorname{argmin}} \frac{1}{N}\sum_{n=1}^{N} \|\Psi \circ \Phi(\dot\gamma_n) - \dot\gamma_n\|^2. \tag{14}$$

Choosing $k << d$, one can interpret the encoder's output $\mathbf{h} = \Phi(\dot\gamma)$ as a compressed latent representation, whose dimensionality is much less than the original size of the image $\dot\gamma$. The decoder Ψ converts $\mathbf{h}$ to an image similar to the original input

$$\Psi \circ \Phi(\dot\gamma) \approx \dot\gamma. \tag{15}$$

For our application of lung imaging using an E-channel EIT system, we choose the class of functions $\mathbb{AE}$ to contain encoder functions Φ of the form

$$\Phi(\dot\gamma) := W^{\ell-1} \circledast \left(\eta\left(W^{\ell-2} \circledast \eta\left(\cdots\eta\left(W^{1} \circledast \dot\gamma\right)\cdots\right)\right)\right) \tag{16}$$

and decoder functions Ψ of the form

$$\Psi(\mathbf{h}) = \tanh\left(W^{2\ell} \circledast^{\dagger} \left(\eta\left(W^{2\ell-1} \circledast^{\dagger} \eta\left(\cdots\eta\left(W^{\ell+1} \circledast^{\dagger} \mathbf{h}\right)\cdots\right)\right)\right)\right). \tag{17}$$

Here, $W \circledast \mathbf{x}$ and $W \circledast^{\dagger} \mathbf{x}$, respectively, are the convolution and transposed convolution [58] of $\mathbf{x}$ with weight W; tanh is the hyperbolic tangent function; η is the rectified linear unit activation function *ReLU*. The dimension k (the number of the latent variables) is chosen to be smaller than $E(E-3)/2$ as motivated in subsection 3.4. We hope that Φ and Ψ satisfy the following.

(P1) $\Psi(\Phi(\dot\gamma_n)) \approx \dot\gamma_n$, i.e., the lung ventilation conductivity images in the training data set approximately lie on the low dimensional manifold

$$\mathcal{M} = \{\Psi(\mathbf{h}) : \mathbf{h} \in \mathbb{R}^k\}.$$

(P2) $\mathcal{M}$ is a manifold of useful lung EIT images. In particular, this means that for two images $\dot\gamma_i = \Psi(\mathbf{h}_i)$ and $\dot\gamma_j = \Psi(\mathbf{h}_j)$ in $\mathcal{M}$, the interpolated image $\Psi((1-t)\mathbf{h}_i + t\mathbf{h}_j)$ should represent a lung EIT image between $\dot\gamma_i$ and $\dot\gamma_j$.

Assuredly, the autoencoder approach aims to fulfill (P1) by minimizing the reconstruction loss of (14). However, the second property (P2), as shown in Figures 3 and 4, may not be satisfied by the classical deterministic autoencoder approach (14). There may be holes in the latent space on which the decoder is never trained [49]. Hence, $\Psi((1-t)\mathbf{h}_i + t\mathbf{h}_j)$ for some t may be an unrealistic lung ventilation image. This is the reason we use variational autoencoder, which can be viewed as a regularized autoencoder or nonlinear principal component analysis [8, 32].

Let us also stress that the mappings Ψ and Φ will only be approximately inverse to each other, so that $\mathcal{M}$ might not be a manifold in the strict mathematical sense. However, the set $\mathcal{M}$ constructed with this approach (also including the VAE approach described in the next subsection) will always be an image of the low dimensional latent space $\mathbb{R}^k$ under the continuous mapping Ψ. For the sake of readability, we keep the somewhat sloppy terminology and refer to $\mathcal{M}$ as a low dimensional manifold. Moreover, note that the image of Ψ of a closed bounded subset of the latent space $\mathbb{R}^k$ will be compact.

3.4.2. Variational autoencoder (VAE). The idea of VAE is to add variations in the latent space to the minimization problem (14) in order to achieve (P2). More precisely, in VAE, the encoder Φ is of the following nondeterministic form:

$$\Phi(\dot{\gamma}) = \Phi_{\text{me}}(\dot{\gamma}) + \Phi_{\text{std}}(\dot{\gamma}) \odot \mathbf{h}_{\text{noise}}, \tag{18}$$

where Φ_{me} outputs a vector of means $\mu = (\mu(1), \ldots, \mu(k)) \in \mathbb{R}^k$; Φ_{std} outputs a vector of standard deviation $\sigma = (\sigma(1), \ldots, \sigma(k)) \in \mathbb{R}^k$; $\mathbf{h}_{\text{noise}}$ is an auxiliary noise variable sampled from standard normal distribution $\mathcal{N}(0, I)$; and $\odot$ is the elementwise product (Hadamard product). Here, Φ_{me} and Φ_{std} are of the form (16) and describe the mean vector $\mu = \Phi_{\text{me}}(\dot{\gamma})$ and the standard variation vector $\sigma = \Phi_{\text{std}}(\dot{\gamma})$ of the nondeterministic encoder function.

According to (18),

$$\Phi(\dot{\gamma}) = \mathbf{h} \sim \mathcal{N}(\mu, \Sigma),$$

where Σ is a diagonal covariance matrix $\Sigma = \operatorname{diag}(\sigma(1)^2, \ldots, \sigma(k)^2)$. With this nondeterministic approach, we can fulfill the property (P2) since the same input $\dot{\gamma}$ can now be encoded as a whole range of perturbations of $\mathbf{h}$ in the latent space, and thus we can determine a decoder function Ψ that maps a whole range of perturbations of $\mathbf{h}$ to useful lung images. To find Ψ, note that for all images $\dot{\gamma}$, the concatenation $\Psi(\Phi(\dot{\gamma}))$ is now a random vector. Since we can also interpret $\dot{\gamma}$ as a random vector which always takes the same value, we could ensure the desired property (P1) by simply minimizing (14) with $\|\cdot\|$ now denoting the energy distance between two random vectors. But this trivial approach would obviously still prefer a deterministic encoder, i.e., Φ_{me} will be the encoder function from the standard autoencoder approach, and $\Phi_{\text{std}} \equiv 0$.

Hence, in order to ensure variations in the latent space to achieve (P2), we additionally enforce that the distribution of the encoder output is close to a normal distribution. We thus minimize (14) with an additional term that penalizes the Kullback–Leibler (KL) divergence loss between $\mathcal{N}(\mu_n, \Sigma_n)$ and $\mathcal{N}(0, I)$ for all $n = 1, \ldots, N$:

$$D_{KL}(\mathcal{N}(\mu_n, \Sigma_n) \parallel \mathcal{N}(0, I)) = \frac{1}{2}\sum_{j=1}^{k} \left[\mu_n(j)^2 + \sigma_n(j)^2 - \log \sigma_n(j) - 1\right]. \tag{19}$$

We thus obtain the VAE method

$$(\Psi, \Phi) = \underset{(\Psi,\Phi)\in\mathbb{VAE}}{\operatorname{argmin}} \frac{1}{N} \sum_{n=1}^{N} \left[\|\Psi \circ \Phi(\dot\gamma_n) - \dot\gamma_n\|^2 + D_{KL}(\mathcal{N}(\mu_n, \Sigma_n) \parallel \mathcal{N}(0, I)) \right], \tag{20}$$

where $\mu_n = \Phi_{\mathrm{me}}(\dot\gamma_n)$ and $\sigma_n = \Phi_{\mathrm{std}}(\dot\gamma_n)$. We should note that the covariance Σ_n and the term $D_{KL}(\mathcal{N}(\mu_n, \Sigma_n) \parallel \mathcal{N}(0, I))$ allow smooth interpolation and compact encoding, resulting in the generation of a compact smooth manifold.

3.5. The image reconstruction algorithm. Now we are ready to explain the reconstruction algorithm f_{EIT}. Given a set of training data, the key idea is that we do not aim to learn a nonlinear regression map that directly reconstructs the conductivity $\dot\gamma$ from the voltage measurements $\dot{\mathbf{V}}$ as this will be a highly underdetermined and ill-posed problem. Instead we first use the variational autoencoder method as explained in the last subsection to identify a low dimensional latent space encoding the manifold of useful lung images and then learn the nonlinear regression map that reconstructs the low dimensional latent variable as this problem can be expected to be considerably better posed.

To explain this in more detail, let $\{(\dot{\mathbf{V}}_n, \dot\gamma_n) : \ n = 1, \dots, N\}$ be a set of training data. Using the learned encoder Φ_{me} in (18), we obtain a set of training data for the latent variable $\{(\dot{\mathbf{V}}_n, \mathbf{h}_n) : n = 1, \dots, N\}$ with

$$\mathbf{h}_n := \Phi_{\mathrm{me}}(\dot\gamma_n). \tag{21}$$

In order to learn a nonlinear reconstruction map that reconstructs the latent variable from the voltage measurements, i.e.,

$$f_{\mathrm{Vh}}(\dot{\mathbf{V}}) \approx \mathbf{h}, \tag{22}$$

we minimize

$$f_{\mathrm{Vh}} = \underset{f_{\mathrm{Vh}}\in\mathbb{DL}_h}{\operatorname{argmin}} \frac{1}{N} \sum_{n=1}^{N} \|f_{\mathrm{Vh}}(\dot{\mathbf{V}}_n) - \mathbf{h}_n\|^2, \tag{23}$$

where $\mathbb{DL}_h$ is the multilayer perceptrons with their mathematical representation given by

$$f^*_{\mathrm{Vh}}(\dot{\mathbf{V}}) = W_\sharp^{\ell-1}\left(\eta\left(W_\sharp^{\ell-2}\left(\cdots\eta\left(W_\sharp^{1}\dot{\mathbf{V}}\right)\cdots\right)\right)\right), \tag{24}$$

where $W_\sharp \mathbf{x}$ is the matrix multiplication of $\mathbf{x}$ with weight $W_\sharp$, and η is $ReLU$. See Figure 5 for details.

After finding f_{Vh} by solving the minimization problem (23), we can reconstruct the conductivity from the latent variable by applying the decoder Ψ in (17). In summary, the proposed lung EIT reconstruction map is

$$f_{\mathrm{EIT}} := \Psi \circ f_{\mathrm{Vh}} : \ \dot{\mathbf{V}} \ \longrightarrow \ \mathbf{h} \ \longrightarrow \ \dot\gamma. \tag{25}$$

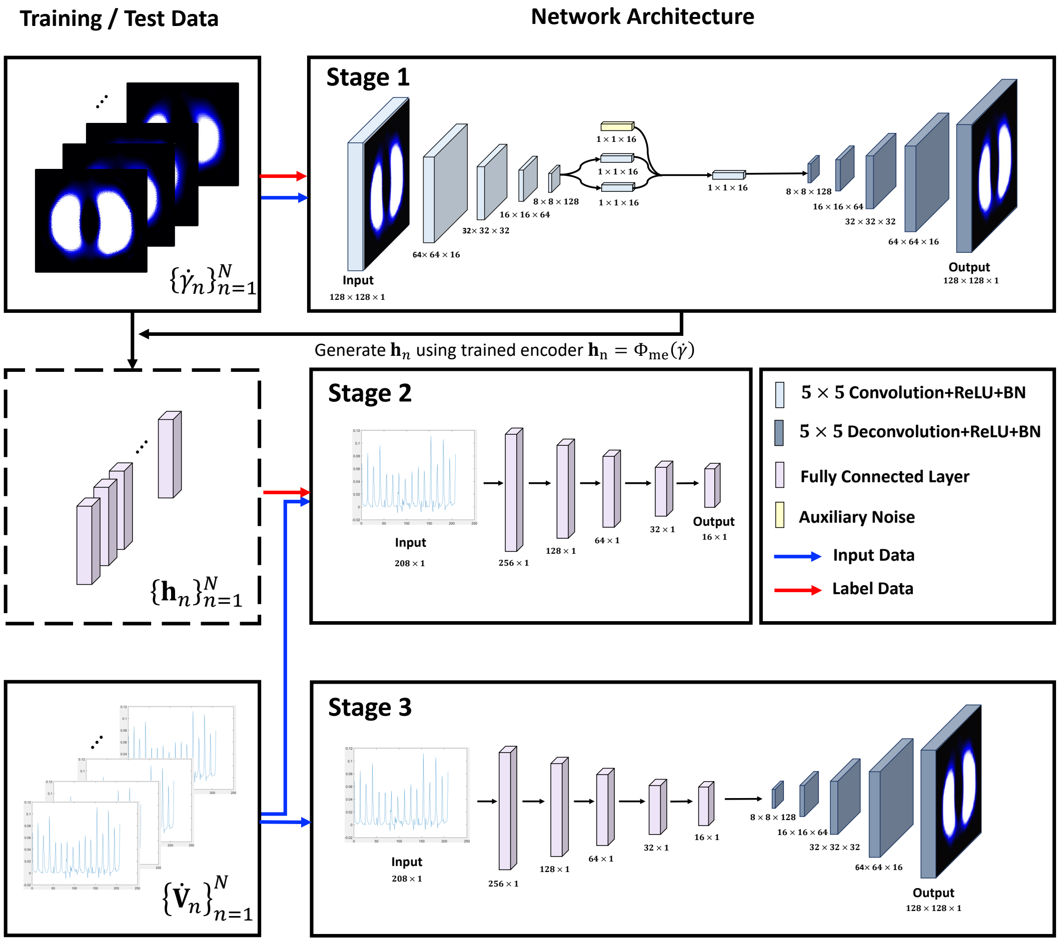

Figure 5. *Architecture of the proposed image reconstruction method. In the first stage, variational autoencoder is used to learn a 16-dimensional manifold representation for getting prior knowledge of lung EIT images. In the second stage, a map* $f_{Vh} : \dot{\mathbf{V}} \to \mathbf{h}$ *is trained with* $\{(\dot{\mathbf{V}}_n, \mathbf{h}_n)\}_{n=1}^N$. *Here* $\mathbf{h}_n$ *were given by encoder;* $\Phi_{me}(\dot{\gamma}_n)$. *In the third stage,* $f_{EIT} := \Psi \circ f_{Vh}^*$ *works with trained* f_{Vh}^* *and* Ψ.

4. Experiments and results.

4.1. Generating labeled data. We numerically generate a set of labeled data $\{(\dot{\mathbf{V}}_n, \dot{\gamma}_n) : n = 1, \dots, N\}$ using the forward model (4) with a 16-channel EIT system and the filtering process in section 3.3. To mimic practical situations, we use some human experiment results by the fidelity-embedded reconstruction method [39] to collect a set of labeled data $\{(\dot{\mathbf{V}}_m, \dot{\gamma}_m) : m = 1, \dots, k\}$. We also interpolate these data to generate additional data by computing the forward problem (4) and (5). The number of training data $\{(\dot{\mathbf{V}}_n, \dot{\gamma}_n) : n = 1, \dots, N\}$ was 21360. For data augmentation purposes, we added 10 different 5% Gaussian random noises to $\dot{\mathbf{V}}$. The size of the images $\dot{\gamma}_n$ is 128×128. All training was performed using an NVIDIA GeForce GTX 1080ti GPU.

4.2. Training procedure and reconstruction result. The proposed method consists of three stages: (i) training variational autoencoder to find a low dimensional representation; (ii) training the nonlinear regression map f_{Vh} from EIT data to latent variables; (iii) EIT image reconstruction.

Algorithm 1. The proposed training and reconstruction algorithm.

```
Stage 1. Training variational autoencoder to find a low dimensional representation
    for number of training step do
        • Sample the minibatch of $m$ image $\{\dot\gamma_1, \dots, \dot\gamma_m\}$ from training data.
        • Sample the minibatch of $m$ auxiliary noise $\{\mathbf{h}_{\mathrm{noise},1}, \dots, \mathbf{h}_{\mathrm{noise},m}\}$ from standard normal $\mathcal{N}(\mathbf{0}, \mathbf{I})$.
        • Update the parameters of VAE using the gradient of the loss $\mathcal{L}_1$ in (20) with respect to the parameters of VAEs for the minibatch:
            $\mathcal{L}_1 = \frac{1}{m} \sum_{n=1}^{m} \left[ \|\Psi \circ \Phi(\dot\gamma_n) - \dot\gamma_n\|^2 + D_{KL}(\mathcal{N}(\mu_n, \Sigma_n) \parallel \mathcal{N}(0, I)) \right]$
    end for
Stage 2. Training the nonlinear regression map $f_{\mathrm{Vh}}$
    for number of training step do
        • Sample the minibatch of $m$ image $\{\dot\gamma_1, \dots, \dot\gamma_m\}$ from training data and encode the sampled images to generate $\{\Phi_{\mathrm{me}}(\dot\gamma_1), \dots, \Phi_{\mathrm{me}}(\dot\gamma_m)\}$.
        • Sample the minibatch of $m$ paired voltage data $\{\dot{\mathbf{V}}_1, \dots, \dot{\mathbf{V}}_m\}$ from training data set.
        • Update the parameters of $f_{\mathrm{Vh}}$ using gradient of loss $\mathcal{L}_2$ in (23) with respect to the parameters of $f_{\mathrm{Vh}}$ for the minibatch:
            $\mathcal{L}_2 = \frac{1}{m} \sum_{n=1}^{m} \|f_{\mathrm{Vh}}(\dot{\mathbf{V}}_n) - \mathbf{h}_n\|^2$
    end for
Stage 3. EIT image reconstruction
    Using the trained nonlinear regression map $f_{\mathrm{Vh}}$ and decoder $\Psi$, an EIT reconstruction map $f_{\mathrm{EIT}}$ is achieved by
        $f_{\mathrm{EIT}}(\dot{\mathbf{V}}) = \Psi \circ f_{\mathrm{Vh}}(\dot{\mathbf{V}})$.
```

We used the AdamOptimizer [31] to minimize loss. The batch normalization [28] was also applied. After finishing the training process (stages 1 and 2), EIT reconstruction images were given by $f_{\mathrm{EIT}}(\dot{\mathbf{V}}) = \Psi \circ f_{\mathrm{Vh}}(\dot{\mathbf{V}})$. The reconstruction result is shown in Figure 6.

4.3. Visualizations of learned manifold. Our experimental result shows that lung EIT images lie on the low dimensional smooth compact manifold. For easy visualization purposes, we visualized the lung EIT manifold with two-dimensional latent space to project the high

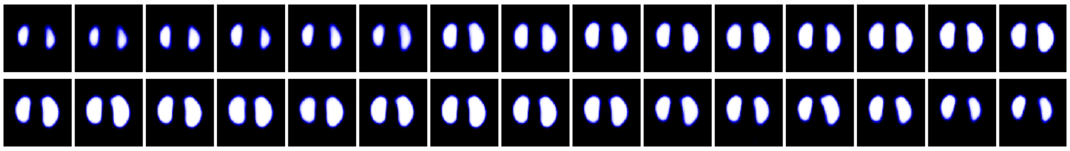

Reconstruction by proposed deep learning-based method

Figure 6. *Reconstruction result of deep learning-based method from real experimental data. The reconstructions were given by* $f_{EIT}(\dot{\mathbf{V}}) = \Psi \circ f_{Vh}(\dot{\mathbf{V}})$.

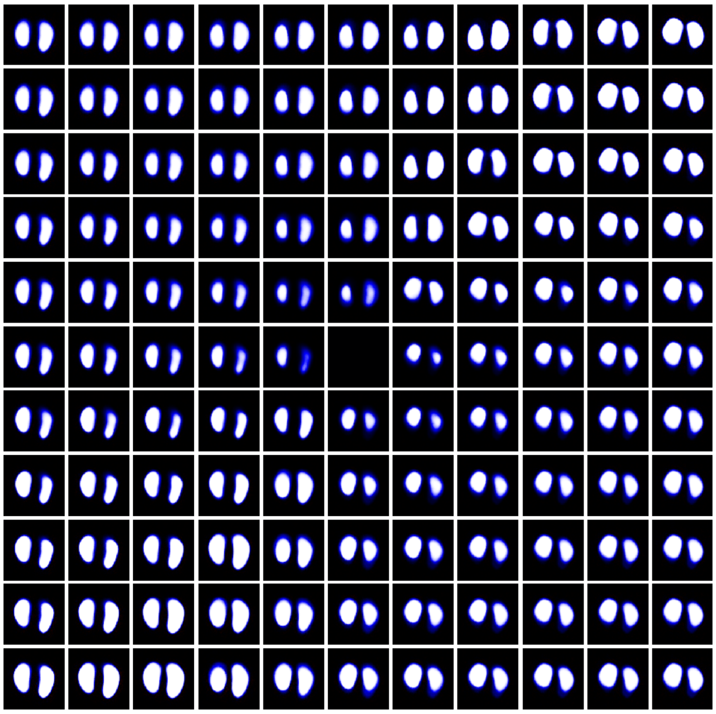

Figure 7. *Visualization of learned lung EIT manifold with two-dimensional latent space.*

dimensional image to the low dimensional manifold. Here we chose the equally spaced latent variables $\mathbf{h} \in [-3,3]^2$, and we decoded them to generate the images as shown in Figure 7.

We also visualized a manifold with 16-dimensional latent space. Since we cannot directly visualize a 16-dimensional manifold, we visualized the manifold along each axis of the 16-dimensional latent space as shown in Figure 8(a). Here, each ith row in Figure 7(a) shows a lung EIT image $\Psi(\mathbf{h}_{i,j})$ with $\mathbf{h}_{i,j} = \delta_j \mathbf{e}_i$, where $\mathbf{e}_i$ is a unit vector whose ith component is one and otherwise zero with $\delta_j \in \{-6,\dots,0,\dots,6\}$ for $i \in \{1,\dots,16\}$ and $j \in \{1,\dots,13\}$. Each (i,j) image in Figure 8(b) shows the tangent which denotes the direction from the (i,j) image to the $(i,j+1)$ image in Figure 8(a) for $i \in \{1,\dots,16\}$ and $j \in \{1,\dots,12\}$. From the manifold visualization, we can verify that change of lung images (e.g., lung ventilations) are observed when we walk in the latent space.

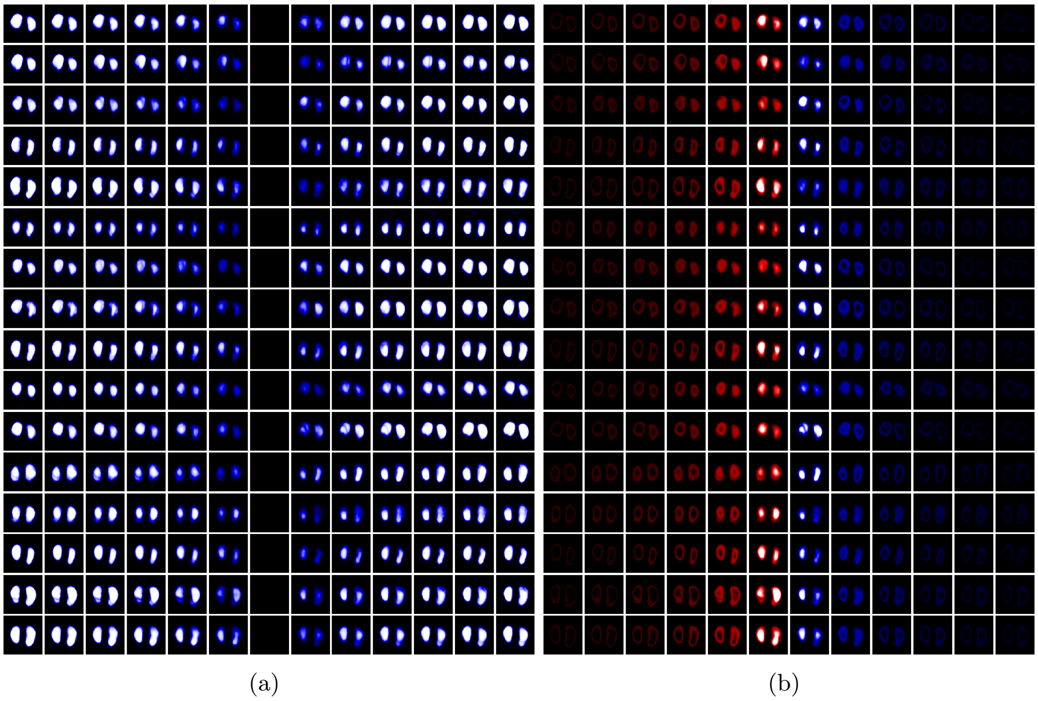
(a) (b)

Figure 8. *Visualization of learned manifold with* 16*-dimensional latent space.* (a) *shows* $\Psi(\mathbf{h}_{i,j})$ *where* $\mathbf{h}_{i,j}$ *have value* $\delta_j \in \{-6, \dots, 6\}$ *in the* i*th component and otherwise zero.* (b) *shows its tangents. We expected that small changes in latent space would produce small changes in image space. Here the blue and red colors denote the positive and negative values.*

4.4. Advantages on VAE-based manifold constraint. The proposed method is more advantageous than conventional regularization methods due to the low dimensional manifold constraint in reconstructing lung images fitting EIT data. The conventional methods do not work for obese people, which is the case in which the lung is placed away from the surface electrodes. The conventional regularization methods may produce merged images due to their fundamental nature, penalizing image perturbation, as shown in Figure 9. On the other hand, the proposed method always generates lung-like images due to the learning constraint of lung images.

In this experiment, we use a simulated image $\dot{\gamma}$ and compute the corresponding simulated data $\dot{\mathbf{V}}$ using the forward model (4) with $\gamma = 1 + \dot{\gamma}$ and a 16-channel EIT system. Here, we added 5% Gaussian random noise to $\dot{\mathbf{V}}$. For each image of $\dot{\gamma}$, 10 different data are computed by adding the noise. In total 21360 ($= 2136 \times 10$) data pairs are used for the training process. The images in Figure 9 compare the proposed method with regularized data fitting methods $\text{argmin}_{\dot{\gamma}} \|\dot{\mathbf{V}} - \mathbb{S}\dot{\gamma}\|^2 + \lambda \|\dot{\gamma}\|_2^2$ by using simulated EIT data. In case 2, as shown in Figure 9, two lungs are merged in the reconstructed images by the regularized data fitting methods, but not in the reconstructed image by the proposed method. This is because the measured data are highly sensitive to conductivity changes near the current-injection electrodes, whereas the sensitivity drops rapidly as the distance increases [7].

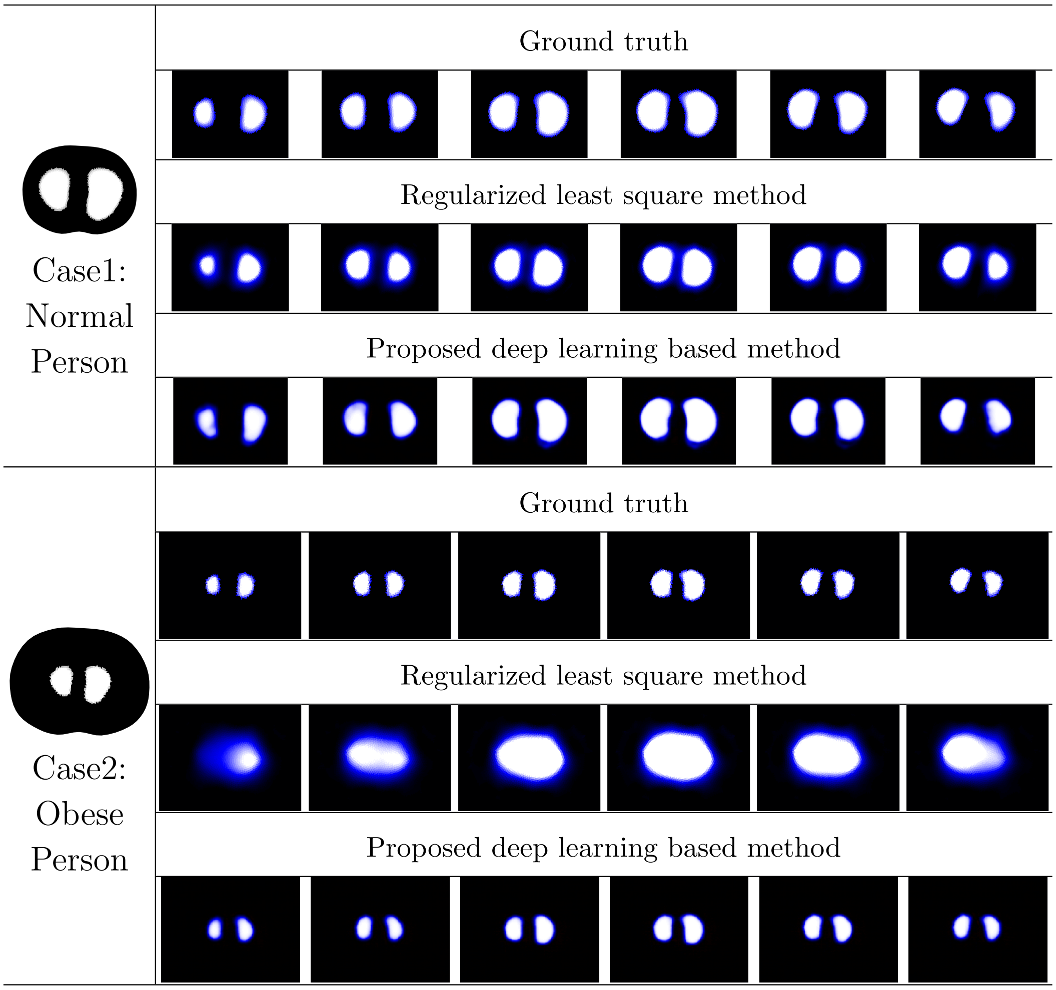

Figure 9. *Comparison of reconstruction methods with simulated data. We compare the proposed deep learning method in section 3 with the standard regularized least square method (10) for two cases: a normal person and an obese person. In case 1 (normal person), both methods produce reasonably accurate reconstructions. In case 2 (obese person), however, the standard method gives a merged image because the electrodes' positions are distant from the support of $\dot{\gamma}$. On the other hand, the proposed method provides useful reconstruction. Here, we resized our result of deep learning to the same ratio of reconstruction of the conventional method for the comparison.*

5. Discussion and conclusion. This paper addresses the problem of handling ill-posed nonlinear inverse problems by suggesting a low dimensional representation of target images. EIT is a typical example of ill-posed nonlinear inverse problems where the dimension of measured data is much lower than the number of unknowns (pixels of the image). Moreover, there exist complicated nonlinear interrelations among inputs (a practical version of Dirichlet-to-Neuman data), outputs (impedance imaging), and system parameters. Finding a robust reconstruction map f_{EIT} for clinical practice requires using prior knowledge on image expression. Regularization techniques have been used widely to deal with ill-posedness, but the conventional L^p-norm-based regularization may not provide a proper prior of target images in practice. See Figure 2.

The deep learning framework may provide a nonlinear regression on training data which acts as learning complex prior knowledge on the output. VAE allows the achievement of compact representation (or low dimensional manifold learning) for prior information of lung EIT images, as shown in Figures 3 and 4. Dai et al. [15] viewed VAE as the natural evolution of robust PCA models, capable of learning nonlinear manifolds of unknown dimension obscured by gross corruptions. Given data $\{\dot{\gamma}_n \in \mathbb{R}^d : \ n = 1, \dots, N\}$, the encoder $\Phi(\dot{\gamma})$ in (18) can be viewed as a conditional distribution $q(\mathbf{h}|\dot{\gamma})$ that satisfies $q(\mathbf{h}|\dot{\gamma}) = \mathcal{N}(\mu, \Sigma)$. The decoder Ψ can be represented by a conditional distribution $p(\dot{\gamma}|\mathbf{h})$ with $p(\mathbf{h}) = \mathcal{N}(0, I)$. VAE tries to match $p(\mathbf{h}|\dot{\gamma})$ and $q(\mathbf{h}|\dot{\gamma})$. VAE encoder covariance can help smooth out undesirable minima in the energy landscape of what would otherwise resemble a more traditional deterministic autoencoder [15].

Given the training data $\{(\dot{\mathbf{V}}_n, \dot{\gamma}_n) : n = 1, \dots, N\}$, the encoding-decoding pair (Φ, Ψ) and the nonlinear regression map f_{Vh} in (23) satisfy the following properties as in the sense of Hadamard [19]:

- *Approximate existence.* Given $\dot{\mathbf{V}}$, there exist $\mathbf{h}$ such that $f_{\mathrm{Vh}}(\dot{\mathbf{V}}) \approx \mathbf{h}$.
- *Approximate uniqueness.* For any two different EIT data $\dot{\mathbf{V}}, \dot{\mathbf{V}}'$, we have $\|\Phi(\dot{\mathbf{V}}) - \Phi(\dot{\mathbf{V}}')\| \gtrsim \|f_{\mathrm{Vh}}(\dot{\mathbf{V}}) - f_{\mathrm{Vh}}(\dot{\mathbf{V}}')\|$.
- *Stability.* $\dot{\mathbf{V}} \approx \dot{\mathbf{V}}'$ implies $\Phi(\dot{\mathbf{V}}) \approx \Phi(\dot{\mathbf{V}}')$.

The proposed deep learning approach is a completely different paradigm from regularized data-fitting approaches that use a “single” data fidelity with regularization. The deep learning approach instead uses a “group” data fidelity to learn an inverse map from the training data. The deep learning framework can provide a nonlinear regression for the training data, which acts as learning complex prior knowledge of the output. Let us explain this using the well-known example of sub-Nyquist sampling (compressive sensing) MRI, which is an ill-posed inverse problem with fewer equations than unknowns. The well-known compressed sensing (CS) method with random sampling is based on the regularized data-fitting approach (single data fidelity), where total variation regularization is used to enforce the image sparsity to compensate for undersampled data [11, 41]. The CS method requires nonuniform random subsampling, since it is effective to reduce noise. On the other hand, the deep learning-based method [27] provides a low dimensional latent representation of MR images, which can be learned from the training set (group data fidelity). The learned reconstruction function from the group data fidelity appears to have highly expressive representation capturing anatomical geometry as well as small anomalies [27].

Deep learning techniques have expanded our ability by sophisticated “disentangled representation learning” though training data. Deep learning methods appear to overcome limitations of existing mathematical methods in handling various ill-posed problems. Deep learning methods will improve their performance as training data and experience accumulate over time. However, we do not have rigorous mathematical evidence for why deep learning methods work so well. We need to develop mathematical theories to ascertain their reliability.

REFERENCES

[1] A. Adler, R. Guardo, and Y. Berthiaume, *Impedance imaging of lung ventilation: Do we need to account for chest expansion?*, IEEE Trans. Biomed. Engrg., 43 (2005), pp. 414–420.

[2] A. Adler and W. R. B. Lionheart, *Uses and abuses of EIDORS: An extensible software base for EIT*, Physiol. Meas., 27 (2006), pp. S25–S42.

[3] G. Alessandrini and S. Vessella, *Lipschitz stability for the inverse conductivity problem*, Adv. Appl. Math., 35 (2005), pp. 207–241.

[4] K. Astala and L. Päivärinta, *Calderón's inverse conductivity problem in the plane*, Ann. of Math. (2), 163 (2006), pp. 265–299.

[5] D. C. Barber, *A sensitivity method for electrical impedance tomography*, Clin. Phys. Physiol. Meas., 10 (1989), pp. 368–369.

[6] D. C. Barber and B. H. Brown, *Applied potential tomography*, J. Phys. E Sci. Instrum., 17 (1984), pp. 723–733.

[7] D. C. Barber and B. H. Brown, *Errors in reconstruction of resistivity images using a linear reconstruction technique*, Clin. Phys. Physiol. Meas., 9 (Sup. A) (1988), pp. 101–104.

[8] Y. Bengio, A. Courville, and P. Vincent, *Representation learning: A review and new perspectives*, IEEE Trans. Pattern Anal. Mach. Intell., 35 (2013), pp. 1798–1828.

[9] B. H. Brown, D. C. Barber, and A. D. Seagar, *Applied potential tomography: Possible clinical applications*, Clin. Phys. Physiol. Meas., 6 (1985), pp. 109–121.

[10] A. P. Calderón, *On an inverse boundary value problem*, in Seminar on Numerical Analysis and Its Applications to Continuum Physics, Sociedade Brasileira de Matemática, Rio de Janeiro, Brazil, 1980, pp. 65–73.

[11] E. J. Candès, J. Romberg, and T. Tao, *Robust uncertainty principles: Exact signal reconstruction from highly incomplete frequency information*, IEEE Trans. Inform. Theory, 52 (2006), pp. 489–509.

[12] M. Cheney, D. Isaacson, J. Newell, S. Simske, and J. Goble, *NOSER: An algorithm for solving the inverse conductivity problem*, Internat. J. Imaging Syst. Tech., 2 (1990), pp. 66–75.

[13] M. Cheney, D. Isaacson, and J. C. Newell, *Electrical impedance tomography*, SIAM Rev., 41 (1999), pp. 85–101, https://doi.org/10.1137/S0036144598333613.

[14] M. K. Choi, B. Bastian, and J. K. Seo, *Regularizing a linearized EIT reconstruction method using a sensitivity-based factorization method*, Inverse Probl. Sci. Eng., 22 (2014), pp. 1029–1044.

[15] B. Dai, Y. Wang, J. Aston, G. Hua, and D. Wipf, *Hidden Talents of the Variational Autoencoder*, preprint, https://arxiv.org/abs/1706.05148, 2018.

[16] C. Doersch, *Tutorial on Variational Autoencoders*, preprint, https://arxiv.org/abs/1606.05908, 2016.

[17] I. Frerichs et al., *Chest electrical impedance tomography examination, data analysis, terminology, clinical use and recommendations: Consensus statement of the translational EIT development study group*, Thorax, 72 (2017), pp. 83–93.

[18] I. Goodfellow, Y. Bengio, and A. Courville, *Deep Learning*, MIT Press, Cambridge, MA, 2016, https://www.deeplearningbook.org.

[19] J. Hadamard, *Sur les problèmes aux dérivées partielles et leur signification physique*, Bull. Univ. Princeton, 13 (1902), pp. 49–52.

[20] M. Hanke and M. Brühl, *Recent progress in electrical impedance tomography*, Inverse Problems, 19 (2003), pp. 1–26.

[21] B. Harrach, *Interpolation of missing electrode data in electrical impedance tomography*, Inverse Problems, 31 (2015), 115008.

[22] B. Harrach, *Uniqueness and Lipschitz stability in electrical impedance tomography with finitely many electrodes*, Inverse Problems, 35 (2019), 024005.

[23] B. Harrach and Y.-H. Lin, *Monotonicity-Based Inversion of the Fractional Schrödinger Equation* II. *General Potential and Stability*, preprint, https://arxiv.org/abs/1903.08771, 2019.

[24] B. Harrach and H. Meftahi, *Global uniqueness and Lipschitz-stability for the inverse Robin transmission problem*, SIAM J. Appl. Math., 79 (2019), pp. 525–550, https://doi.org/10.1137/18M1205388.

[25] R. P. Henderson and J. G. Webster, *An impedance camera for spatially specific measurements of the thorax*, IEEE Trans. Biomed. Engrg., 25 (1978), pp. 250–254.

[26] D. S. Holder, *Electrical Impedance Tomography: Methods, History and Applications*, IOP Publishing, Bristol, UK, Philadelphia, 2005.

[27] C. M. Hyun, H. P. Kim, S. M. Lee, S. Lee, and J. K. Seo, *Deep learning for undersampled MRI reconstruction*, Phys. Med. Biol., 63 (2018), 135007.

[28] S. Ioffe and C. Szegedy, *Batch Normalization: Accelerating Deep Network Training by Reducing Internal Covariate Shift*, preprint, https://arxiv.org/abs/1502.03167, 2015.

[29] D. Isaacson, *Distinguishability of conductivities by electric current computed tomography*, IEEE Trans. Med. Imag., 5 (1986), pp. 91–95.

[30] C. Kenig, J. Sjöstrand, and G. Uhlmann, *The Calderón problem with partial data*, Ann. of Math. (2), 165 (2007), pp. 567–591.

[31] D. P. Kingma and J. L. Ba, *Adam: A Method for Stochastic Optimization*, preprint, https://arxiv.org/abs/1412.6980, 2014.

[32] D. P. Kingma and M. Welling, *Auto-Encoding Variational Bayes*, preprint, https://arxiv.org/abs/1312.6114, 2013.

[33] A. Kirsch, *Characterization of the shape of a scattering obstacle using the spectral data of the far field operator*, Inverse Problems, 14 (1998), pp. 1489–1512.

[34] R. Kohn and M. Vogelius, *Determining conductivity by boundary measurements*, Comm. Pure Appl. Math., 37 (1984), pp. 113–123.

[35] R. V. Kohn and M. Vogelius, *Determining conductivity by boundary measurements* II. *Interior results*, Comm. Pure Appl. Math., 38 (1985), pp. 643–667.

[36] V. Kolehmainen, M. Vauhkonen, P. A. Karjalainen, and J. P. Kaipio, *Assessment of errors in static electrical impedance tomography with adjacent and trigonometric current patterns*, Physiol. Meas., 18 (1997), pp. 289–303.

[37] C. J. Kotre, *A sensitivity coefficient method for the reconstruction of electrical impedance tomograms*, Clin. Phys. Physiol. Meas., 10 (1989), pp. 275–281.

[38] Y. LeCun, Y. Bengio, and G. Hinton, *Deep learning*, Nature, 521 (2015), pp. 436–444.

[39] K. Lee, E. J. Woo, and J. K. Seo, *A fidelity-embedded regularization method for robust electrical impedance tomography*, IEEE Trans. Med. Imag., 37 (2017), pp. 1970–1977.

[40] W. R. B. Lionheart, *EIT reconstruction algorithms: Pitfalls, challenges and recent developments*, Physiol. Meas., 25 (2004), pp. 125–142.

[41] M. Lustig, D. L. Donoho, and J. M. Pauly, *Sparse MRI: The application of compressed sensing for rapid MR imaging*, Magn. Reson. Med., 58 (2007), pp. 1182–1195.

[42] T. Meier et al., *Assessment of regional lung recruitment and derecruitment during a PEEP trial based on electrical impedance tomography*, Intensive Care Med., 34 (2008), pp. 543–550.

[43] P. Metherall, D. C. Barber, R. H. Smallwood, and B. H. Brown, *Three-dimensional electrical impedance tomography*, Nature, 380 (1996), pp. 509–512.

[44] J. L. Mueller and S. Siltanen, *Linear and Nonlinear Inverse Problems with Practical Applications*, Comput. Sci. Engrg. 10, SIAM, Philadelphia, 2012, https://doi.org/10.1137/1.9781611972344.

[45] J. L. Mueller, S. Siltanen, and D. Isaacson, *A direct reconstruction algorithm for electrical impedance tomography*, IEEE Trans. Med. Imag., 21 (2002), pp. 555–559.

[46] A. Nachman, *Reconstructions from boundary measurements*, Ann. of Math. (2), 128 (1988), pp. 531–576.

[47] A. Nachman, *Global uniqueness for a two-dimensional inverse boundary problem*, Ann. of Math. (2), 143 (1996), pp. 71–96.

[48] C. Putensen, H. Wrigge, and J. Zinserling, *Electrical impedance tomography guided ventilation therapy*, Critical Care, 13 (2007), pp. 344–350.

[49] P. K. Rubenstein, B. Schoelkopf, and I. Tolstikhin, *On the Latent Space of Wasserstein Auto-Encoders*, preprint, https://arxiv.org/abs/1802.03761, 2018.

[50] F. Santosa and M. Vogelius, *A backprojection algorithm for electrical impedance imaging*, SIAM J. Appl. Math., 50 (1990), pp. 216–243, https://doi.org/10.1137/0150014.

[51] B. Schullcke, B. Gong, S. Krueger-Ziolek, M. Soleimani, U. Mueller-Lisse, and K. Moeller, *Structural-functional lung imaging using a combined CT-EIT and a Discrete Cosine Transformation reconstruction method*, Nature Sci. Rep., 6 (2016), 25951.

[52] J. K. Seo and E. J. Woo, *Nonlinear Inverse Problems in Imaging*, Wiley, New York, 2013.

[53] S. Siltanen, J. Mueller, and D. Isaacson, *An implementation of the reconstruction algorithm of A. Nachman for the 2D inverse conductivity problem*, Inverse Problems, 16 (2000), pp. 681–699.

[54] E. Somersalo, M. Cheney, D. Isaacson, and E. Isaacson, *Layer stripping: A direct numerical method for impedance imaging*, Inverse Problems, 7 (1991), pp. 899–926.

[55] J. Sylvester and G. Uhlmann, *A global uniqueness theorem for an inverse boundary value problem*, Ann. of Math. (2), 125 (1987), pp. 153–169.

[56] A. N. Tikhonov and V. Y. Arsenin, *Solutions of Ill-Posed Problems*, H. Winston & Sons, Washington, DC, 1977.

[57] T. Yorkey, J. Webster, and W. Tompkins, *Comparing reconstruction algorithms for electrical impedance tomography*, IEEE Trans. Biomed. Engrg., 34 (1987), pp. 843–852.

[58] M. D. Zeiler and R. Fergus, *Visualizing and Understanding Convolutional Networks*, preprint, https://arxiv.org/abs/1311.2901, 2013.

[59] J. Zhang and R. P. Patterson, *EIT images of ventilation: What contributes to the resistivity changes?*, Physiol. Meas., 26 (2005), pp. S81–S92.

[60] L. Zhou, B. Harrach, and J. K. Seo, *Monotonicity-based electrical impedance tomography for lung imaging*, Inverse Problems, 34 (2018), 045005.